Effect of surface preparation by high-temperature hydrogen annealing on the passivation of Ni-20 at.% Cr alloy in sulfuric acid

Junsoo Han, Shova Neupane, Luntao Wang, Antoine Seyeux, Lorena Klein, Sandrine Zanna, Dimitri Mercier, Vincent Maurice, Philippe Marcus

Highlights

- Investigation of native and passive surface films formed on Ni-20 at.% Cr alloy surfaces
- Surface analysis by *in situ* electrochemical measurements combined with advanced *ex situ* surface analysis
- Mechanistic understanding of the effects of high-temperature hydrogen annealing pretreatment
- Enhanced corrosion resistance of electrochemically passivated surface by high-temperature hydrogen annealing pretreatment
- Increase in Cr enrichment of initially weakly protected sites of the inner barrier layer

Effect of surface preparation by high-temperature hydrogen annealing on the passivation of Ni-20 at.% Cr alloy in sulfuric acid

[a,b]Junsoo Han, [a,c]Shova Neupane, [a,d]Luntao Wang, [a]Antoine Seyeux, [a]Lorena Klein, [a]Sandrine Zanna, [a]Dimitri Mercier, [a]Vincent Maurice, [a]Philippe Marcus

[a] PSL University, CNRS-Chimie ParisTech, Institut de Recherche Chimie Paris (IRCP), Physical Chemistry of Surfaces Group, 75005 Paris, France
[b] Sorbonne Université, CNRS, Laboratoire Interfaces et Systèmes Electrochimiques (LISE), 75005 Paris, France
[c] Department of Mechanical and Electrical Engineering, University of Southern Denmark, 5220 Odense, Denmark
[d] Institute for Corrosion Multiphase Technology, Ohio University, Athens OH 45701, USA

Abstract

The effect of high-temperature annealing under hydrogen gas surface preparation on a binary polycrystalline Ni-20 at.% Cr alloy was investigated in comparison with conventional mechanical grinding surface preparation. Duplex surface films with inner Cr(III) oxide and outer Ni(II) and Cr(III) hydroxide layers natively formed before and after H_2 annealing were characterized by X-ray photoelectron spectroscopy and time-of-flight secondary ion mass spectroscopy. A thinner and less homogeneous inner barrier layer formed after H_2 annealing caused an oxidation peak at the active/passive transition in the linear sweep voltammetry measurement in a 0.5 M H_2SO_4 solution. Despite this high oxidation peak, passivation of the H_2 annealed surface resulted in the formation of a more corrosion resistant inner layer than on the mechanically ground surface, as demonstrated by electrochemical impedance spectroscopy. The corrosion resistant passive film formation of the H_2 annealed surface is attributed to the increased Cr enrichment of the inner layer caused by the selective Ni dissolution providing corrosion resistance to the initially weakly protected sites of the natively formed surface film.

Keywords: High-temperature hydrogen annealing; Ni-Cr alloys; passivation; XPS; ToF-SIMS; EIS

Corresponding authors: Junsoo Han (junsoo.han@sorbonne-universite.fr), Dimitri Mercier (dimitri.mercier@chimieparistech.psl.eu), Philippe Marcus (philippe.marcus@chimieparistech.psl.eu)

Introduction

Stainless steels and Ni-based Cr-containing alloys are prepared by mechanical grinding before most of the laboratory analysis mainly to obtain a reproducible surface, and sometimes to have a better corrosion resistance [1, 2]. In the case of coated or plated materials, the performance of an alloy system is significantly influenced by the surface preparation method which gives a better adhesion property of the materials to the substrate when properly prepared. Recently developed alloys such as multi-principal element alloys and additively manufactured stainless steels are also generally prepared in the same ways as conventional alloys. An important question is whether the applied surface preparation procedure yields a reproducible and representative surface without significantly altering the surface chemistry, which could further affect the oxidation/corrosion properties. Although several works have referred to the importance of the surface preparation on surface film formation and overall corrosion kinetics [3], it is difficult to suggest a standardized surface preparation method (*i.e.*, polishing or physical grinding) as the surface reactivity also depends on the history of the sample [4, 5, 6, 7]. It is further complicated to predict the effect of surface preparation for the new classes of alloys due to their multi-element, multi-phase nature and their more complex microstructure than for conventional alloys [8, 9]. For example, surface grinding using Si-C papers of a highly rough and geometrically complex as-printed additively manufactured 316L stainless steel did not efficiently remove tortuous asperities that are known to be initiation sites of pitting corrosion [10]. In this case, investigating the effect of surface preparation for relatively simple Fe- or Ni-based Cr-containing binary/ternary alloy systems is useful as a reference for the more complex alloy systems because their passivity, oxidation mechanism and corrosion resistance are relatively well documented [11, 12, 13, 14, 15, 16, 17, 18, 19, 20, 21].

For the Ni-Cr binary system, theoretical calculations combined with laboratory experiments have demonstrated that the general oxidation kinetics strongly depends on the alloy composition, the gaseous or aqueous environment, and the oxidation temperature [18, 19, 22, 23, 24, 25, 26, 27]. Element-resolved characterization analysis has been performed to better understand the early-stage oxidation mechanisms at

the metal/oxide interface that may regulate the overall passivation/corrosion process [17, 18, 28]. The effect of surface preparation on the overall oxidation process and the underlying mechanisms of this relatively simple binary system has, however, not been elucidated to a satisfactory level to date. An in-depth analysis of the effect of surface preparation of this Ni-Cr binary system can be used to better understand the surface film of more complex Ni/Cr containing alloys such as Hastelloy, Inconel, stainless steels, and multi-principal element alloys.

Ni-Cr alloys are known to form a duplex oxide/hydroxide surface layer upon spontaneous passivation and anodic polarization in acidic solutions. The Cr-rich inner oxide layer is known to promote corrosion resistance [15, 17, 19, 29, 30], and the outer layer has been reported to be composed of Ni and Cr hydroxides [29, 31]. Native oxide/hydroxide films form immediately after surface preparation of Ni-based alloys [32, 33], stainless steels, [12, 34], multi-principal element alloys [35, 36] and additively manufactured alloys [37, 38]. The property of this native film is often considered as a key to controlling the corrosion mechanism when the surface is subsequently exposed to corrosive environments (*i.e.*, in acidic solutions) [39, 40, 41]. The important point is that surface preparation may cause significant changes in both the composition and chemical stability of the native film [5, 42], thereby influencing the corrosion resistance of a system [43, 44]. To this end, it is essential to better understand the effect of surface preparation on the composition, structure and thickness of the native films formed on the alloy substrates.

For the surface preparation, mechanical grinding is often followed by electropolishing to further improve the surface quality of the specimen by dissolving active sites such as non-metallic inclusions (*e.g.*, MnS for stainless steels) and by removing the cold-worked layer leftover from grinding. Electropolishing has been reported to provide better resistance to pitting corrosion by reducing surface roughness [45, 46]. The reduced corrosion resistance of an electropolished stainless steel was attributed to the presence of sulfates and phosphates in the passive film observed by X-ray photoelectron spectroscopy (XPS) [45]. However, electropolishing is highly sensitive to the operating parameters [10] which may

lead to a significant increase in the electropolished surface area and possible associated defects [47]. It is a general challenge to accurately control the sample surface after polishing and there is no universal methodology applied to all different alloy systems.

High-temperature annealing is often carried out to improve the mechanical properties of the cold-worked surface layer left from mechanical grinding. Annealing in air carried out under atmospheric oxygen partial pressure results in grain growth by recrystallization of the microstructure. In most cases, however, the surface oxidizes during the high-temperature annealing even at low oxygen partial pressure or during sample transfer for quenching. Moreover, the possible formation of oxide inclusions at the interface in the presence of oxygen may block the cohesive bond in the case of annealing in air [48]. Annealing is also performed in a reducing environment controlled by an inert gas (*e.g.*, H_2) to protect the sample surface from oxidation [49]. This procedure provides stress relief by recrystallizing the cold-worked surface without causing significant damage. The stumbling block of using high-temperature annealing as a surface preparation finish is the uncertainty of the annealing parameters which may cause undesirable surface change [20, 21, 49]. In the case of stainless steels, air-annealing has been reported to lead to the formation and precipitation of the σ-phase at grain boundaries during the heat treatment, known to be detrimental to the corrosion resistance as it may result in Cr and/or Mo depletion in the passive film [50, 51]. For annealing under H_2 atmosphere at T = 1100°C for stainless steel, cracks were observed with the ε-martensite transformation on top of the sample surface attributed to hydrogen ingress during annealing and residual stress during subsequent cooling [49]. Regarding the passivation mechanisms and resulting corrosion resistance of stainless steel and Ni-Cr alloys, only limited information is available to date. On a 316L stainless steel, annealing under a H_2 atmosphere at T = 900°C has proven to be effective in completely recrystallizing the cold-worked layer leftover from mechanical grinding without significantly altering the electrochemical response during passivation in a 0.05 M H_2SO_4 solution [43].

In this work, we present the effect of the H_2 annealing at T = 800°C on a polycrystalline Ni-20 at.% Cr alloy. One set of sample surface was only mechanically ground, and the other set was H_2 annealed after mechanical grinding. The sample surfaces after each preparation method as well as after electrochemical passivation were characterized by XPS and time-of-flight secondary ion mass spectrometry (ToF-SIMS). The effect of H_2 annealing on the passivity of the Ni-20 at.% Cr alloy was investigated by electrochemical measurements, including potentiodynamic polarization, potentiostatic hold at a given potential in the passive domain, and following potentiostatic electrochemical impedance spectroscopy (EIS). The formation of a more corrosion resistant passive film for the H_2 annealed case than for the mechanically ground sample was demonstrated by a combination of *in situ* electrochemical analysis and *ex situ* element-resolved surface characterization. The mechanistic understanding investigated in this work can provide useful insights into the change in surface chemistry caused by the surface finish and how the corrosion resistance provided by the passive film is affected.

Experimental

Materials and sample preparation

Polycrystalline Ni-20 at.% Cr alloy was produced from pure Ni and Cr (purity > 99.95%) by electromagnetic induction melting in a water-cooled Cu crucible under He. The sample surface was ground with SiC paper up to P4000 under deionized (DI) water (Millipore™, 18.2 Ω cm), and then with diamond suspension down to 0.25 µm. The samples were successively cleaned in an ultrasonic bath with acetone, ethanol, and DI water for 2 min each, then dried with flowing Ar gas. After mechanical grinding, another series of samples underwent H_2 annealing at atmospheric pressure and T = 800°C for 8 h. The sample was placed in a quartz tube under vacuum below 10^{-5} mbar to reduce the presence of oxygen and water vapor, and thus prevent the formation of oxides during annealing. After vacuum pumping, a stream of ultrapure H_2 (99.999%, 6 N) gas was introduced into the quartz tube at atmospheric pressure. A furnace

was placed close to the quartz tube and the temperature was ramped to T = 800°C and maintained at this temperature for 8 h. After H_2 annealing, the quartz tube was rapidly quenched with iced water (T ≈ 0°) under H_2 flux and maintained for 1 h to ensure cooling down to ambient temperature before transferring the sample to air.

X-ray photoelectron spectroscopy (XPS)

The sample surface was characterized by a Thermo Electron ESCALAB 250™ spectrometer using a monochromatic Al Kα X-ray source (hυ = 1486.6 eV) under a pressure lower than 10^{-9} mbar. The spectrometer was calibrated with Au $4f_{7/2}$ at 84.1 eV. The photoelectron take-off angle was set at 90°. The high-resolution spectra of Ni 2p, Cr 2p, O 1s and C 1s were recorded at a pass energy of 20 eV with a 0.1 eV step size. The core level spectral decomposition was carried out *via* Avantage™ software using Shirley-type background subtraction.

Time-of-flight secondary ion mass spectrometry (ToF-SIMS)

A dual-beam ToF-SIMS (Iontof™ GambH, Münster, Germany) was utilized to obtain elemental depth profile of the sample. Data acquisition and processing were carried out *via* IONSPEC 6.5™ software. The ToF-SIMS depth profiles were acquired under 10^{-8} mbar by interlaced analysis under static SIMS conditions with sputtering using two ion beams impinging the surface at 45°. A pulsed Bi^+ primary ion beam, delivering a current of 1.2 pA and rastering an area of 100 x 100 μm^2, was used for static SIMS analysis, and a Cs^+ ion gun of 0.5 keV delivering a current of 17 nA over an area of 300 x 300 μm^2 was used for sputtering. The two ion beams were well-aligned to ensure analysis from the center of the sputtered crater. Negative secondary ions were recorded as they are more sensitive to oxide matrices. The Ni_2^-, $NiO_2H_2^-$, $CrO_3H_2^-$, and CrO_2^- secondary ions were selected as characteristic anions of metallic Ni, Ni and Cr hydroxides and Cr oxide, respectively, and their intensities were plotted versus sputtering time to

obtain the depth profiles. The surface film/metal interface was determined from the sputtering time when the Ni_2^- signal reached 80% of its maximum intensity [52].

Electrochemical measurements

A Gamry Reference 600+™ potentiostat was used to perform the electrochemical tests. All the electrochemical measurements were carried out in a conventional 3-electrode electrochemical cell using a saturated calomel electrode (SCE) as reference electrode and a gold wire as counter electrode. A 0.5 M H_2SO_4 solution was prepared from analytical grade materials and DI water. The electrolyte was bubbled with flowing Ar gas for 20 min prior to the experiments. The linear sweep voltammetry (LSV) was performed as follows: measurement of open circuit potential (OCP) for 600 s; then LSV from -0.25 V vs. OCP to 1.1 V vs. SCE with a scan rate of 1 mV s^{-1}. The potentiostatic passivation experiment was conducted at a constant potential of 0.25 V vs. SCE for 4 h after open circuit measurement for 600 s. The passivation potential was chosen from the LSV result. After the potentiostatic hold experiment, EIS was performed at the same potential in the frequency range of 10^5 to 10^{-2} Hz, and the data were recorded with 8 points per decade by a sinusoidal perturbation of 10 mV_{rms}. All EIS spectra were corrected by electrolyte resistance (R_e) determined from Nyquist plots at high-frequency limit. For EIS data analysis, the double layer capacitance (C_{dl}) was also corrected to separate the effect of C_{dl} on the total effective capacitance (C_{eff}) of the interface. The C_{dl} was determined using Brug's relation [53] as:

$$C_{dl} = Q_{dl}^{(1/\alpha_{dl})} (1/R_e + 1/R_{ct})^{(\alpha_{dl} - 1)/\alpha_{dl}} \quad [1]$$

where C_{dl} and Q_{dl} (CPE parameter for the double layer) were obtained from the graphical impedance analysis [54, 55] and the power-law model in the low-frequency domain. R_{ct} is the charge-transfer resistance. The $1/R_{ct}$ term in **Eq. 1** is often negligible because $1/R_{ct} << 1/R_e$. The total impedance was corrected considering the double layer contribution [55] as:

$$Z_{corrected}(\omega) = Z(\omega) - 1/\{(j\omega)^{\alpha_{dl}} Q_{dl}\} \quad [2]$$

The total capacitance of the system was also corrected considering the double layer and electrolyte resistance as:

$$C_{corrected}(\omega) = 1/\{j\omega (Z_{corr}(\omega) - R_e)\} \quad [3]$$

The effective capacitance of the oxide layer (C_δ) was determined using the Cole-Cole representation of the real and imaginary capacitance [56] of $C_{corrected}$ in the high-frequency limit of the real component capacitance. The film thickness (δ) was estimated as:

$$\delta = \varepsilon \varepsilon_0 / C_\delta \quad [4]$$

where ε is the dielectric constant of the film and ε_0 is the vacuum permittivity (8.85×10^{-14} F cm^{-2}). All experiments presented in this work were repeated at least three times and showed good reproducibility.

Results

ToF-SIMS depth profile after each surface preparation

The ToF-SIMS depth profiles of both surface preparations are shown in **Fig. 1**. To simplify the comparison, the mechanically ground sample is denoted M, and the H_2 annealed sample following mechanical grinding is denoted MH. The metal/oxide interfaces were determined by a sputtering time when the Ni_2^- signal reaches 80% of its maximum intensity [34, 52], 17.7 s for M and 20.5 s for MH, respectively. For both surface preparation methods, the maximum intensities of the $CrO_3H_2^-$ and $NiO_2H_2^-$ representing Cr and Ni hydroxides, respectively, are reached prior to the maximum intensity of the CrO_2^- representing Cr oxide. This is a characteristic of a bilayer film formation with an outer layer of Cr and Ni hydroxides mixture and an inner layer mainly of Cr oxide, as previously reported [19]. In **Fig. 1**, the interface between the outer and inner layers is indicated where the $NiO_2H_2^-$ and $CrO_3H_2^-$ intensities start

to decrease from the maximum value. Note that the NiO^- spectra are not presented herein because no Ni(II) oxide peak was observed by XPS curve fitting, as shown in the following section.

It should be also noted that a pseudo intensity plateau of the Ni_2^- signal is observed in the inner layer of the MH sample (7 s < t < 14 s in **Fig. 1(b)**) whereas a continuous increase of the Ni_2^- signal towards its maximum level is observed for the M sample (**Fig. 1(a)**). This pseudo Ni_2^- intensity plateau suggests the formation of an inner layer less homogeneous in thickness for the native surface film reformed after H_2 annealing than for that formed after mechanical grinding. The pseudo plateau observed in the Ni_2^- signal (characteristic species of the metallic substrate) mainly results from the formation of a less homogeneously thick Cr-rich inner layer on the MH sample surface [57, 58]. While the initial native surface film formed after mechanical grinding is reduced under the H_2 environment during high-temperature annealing, a new native surface film may be formed by reoxidation, possibly during quenching due to the presence of oxygen/water vapor in the H_2 stream or during sample transfer in ambient air, similar to previous observations on FeCr, FeCrNi alloys and 316L stainless steel [20, 21, 43, 58]. The surface microstructure (not shown here) of the MH sample recrystallized to the metallic state at high temperature would favor the formation of this less homogeneously thick Cr-rich inner oxide layer at lower temperature, probably due to the decrease in the number of nucleation sites for selective Cr oxidation [11].

For both the M and MH samples, the intensity of the $NiO_2H_2^-$ signal is higher than that of the $CrO_3H_2^-$ signal (**Fig. 1)**. At the outer and inner layer interface, the $NiO_2H_2^-$/ $CrO_3H_2^-$ intensity ratio is 4.2 for the M sample and 2.6 for the MH sample. This indicates that more Ni hydroxide species were formed in the outer layer of the initial native surface film formed after mechanical grinding (M sample) than after reoxidation following H_2 annealing (MH sample), in agreement with the XPS results discussed in the next section.

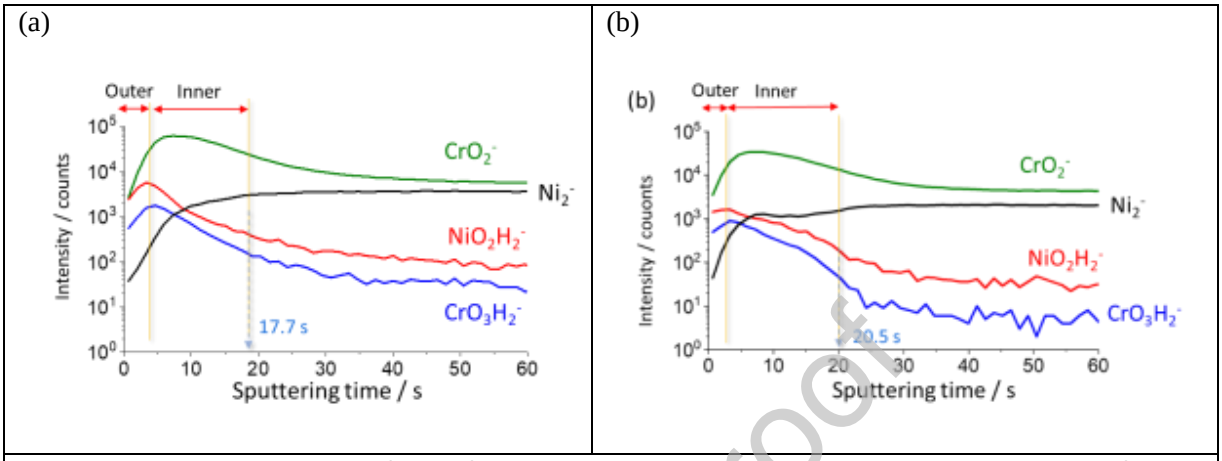

Fig. 1. ToF-SIMS depth profiles of negative ions CrO_2^-, $CrO_3H_2^-$, $NiO_2H_2^-$, and Ni_2^- for **(a)** mechanically ground (M) and **(b)** H_2 annealed (MH) samples.

High-resolution XPS spectra after each surface preparation

The high-resolution Cr 2p, Ni $2p_{3/2}$ and O 1s core level XPS spectra obtained for both surface preparation methods are presented in **Figs. 2**, **3**, and **4**, respectively. The Cr 2p core level spectra in **Fig. 2** were fitted using 3 doublet peaks associated with the Cr $2p_{3/2}$ and Cr $2p_{1/2}$ spin-orbits [59]. The area ratio of the $2p_{1/2}$ peaks to the $2p_{3/2}$ peaks was fixed at the value of 0.5, characteristic of the 2p spin-orbit coupling. Binding energies at 574.1 eV and 583.3 eV; 576.3 eV and 586.3 eV; 577.4 eV and 587.1 eV are attributed to metallic Cr (Cr(0)); Cr(III) oxide; and Cr(III) hydroxide species, respectively [19]. **Fig. 3** presents the Ni $2p_{3/2}$ core level spectra decomposed with 4 components. Binding energies at 852.7 and 858.5 eV are characteristic of metallic Ni (Ni(0)) and the associated satellite, respectively; and peaks at 856.3 and 861.7 eV are associated with the Ni(II) hydroxide principal peak and the associated satellite, respectively [19]. No principal peak could be characterized at 853.7 eV, showing that the presence of Ni(II) oxide in the surface films is below the detection limit. In **Fig. 4**, the O 1s spectra were fitted with 3 components at 530.0 eV (O^{2-}), 531.6 eV (OH^-), and 533.1 eV (H_2O) [19]. For all non-metallic peaks, a

symmetrical shape is observed with the exception of Cr(III) in Cr_2O_3 which shows an asymmetrical shape due to a discrete multiplet structure [19]. For the metallic peaks, an asymmetrical function was used for fitting. It is shown that the native surface films are composed of Cr(III) and Ni(II) hydroxide species in the outer layer and of Cr(III) oxide species in the inner layer based on combined XPS and ToF-SIMS characterizations.

Fig. 2 shows that the intensity ratio between Cr(III) and Cr(0) is significantly higher for the M than for the MH sample. This observation confirms that the H_2 annealing effectively reduces the initial Cr-rich native surface film formed after mechanical grinding. The Cr(III) peaks observed for the MH sample are most probably due to the surface reoxidation after reduction at high temperature as discussed above. The lower Cr(III)/Cr(0) intensity ratio for the MH sample indicates that the reformed native surface film is thinner and/or less Cr-enriched than the initial native surface film formed after mechanical grinding.

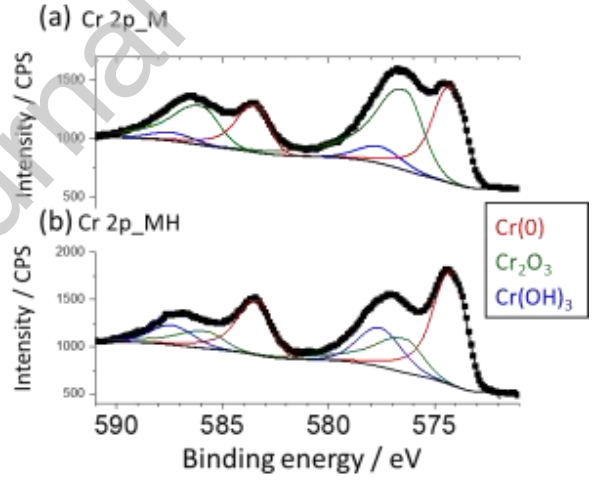

Fig. 2. High-resolution XPS Cr 2p core level spectra for **(a)** mechanically ground (M) and **(b)** H_2 annealed (MH) samples.

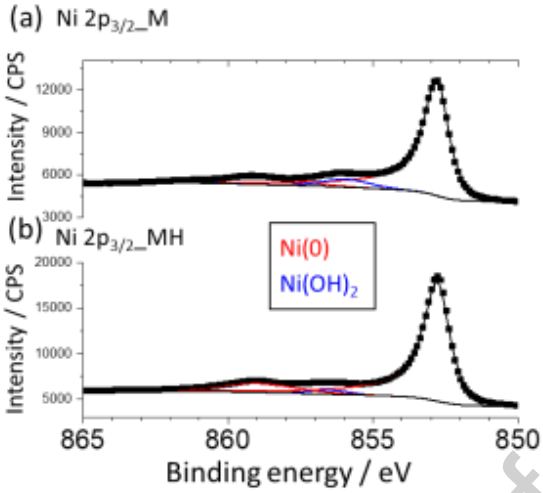

Fig. 3. High-resolution XPS Ni $2p_{3/2}$ core level spectra for **(a)** mechanically ground (M) and **(b)** H_2 annealed (MH) samples.

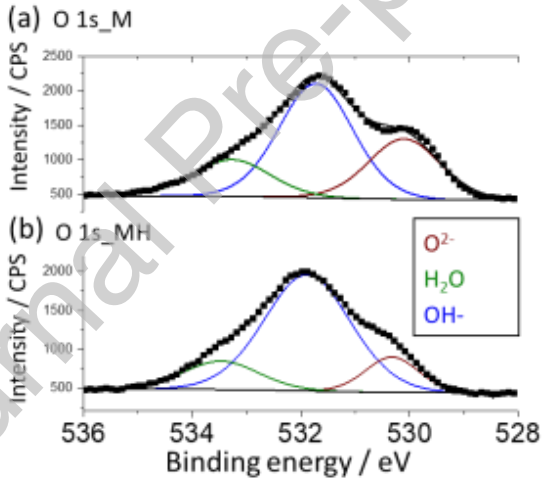

Fig. 4. High-resolution XPS O 1s core level spectra for **(a)** mechanically ground (M) and **(b)** H_2 annealed (MH) samples.

The composition and thickness of the surface films as well as the composition of the underlying alloy substrate were estimated using a layered surface film model taking into account of the attenuation of photoelectron intensities [32, 52]. The results obtained for both surface preparation methods are provided in **Table 1**. A bilayer model [32] was used assuming an inner layer consisting of Cr_2O_3 and an outer layer

consisting of $Cr(OH)_3$ and $Ni(OH)_2$ in agreement with the ToF-SIMS and XPS results for both the M and MH samples. The calculated total equivalent thickness is 0.8 nm for the M sample with 0.5 nm of inner layer and 0.3 nm of outer layer. For the MH sample, the results must be considered with more caution since the applied model considers layers that are homogeneous in thickness and composition. The calculated total equivalent thickness of the MH sample is 0.5 nm with 0.3 and 0.2 nm of inner and outer layers, respectively, which provides a basis for comparison to discuss the effect of the H_2 annealing treatment. Schematic images describing the surface after each surface preparation are provided in **Fig. 5**.

The thinner inner and outer layers formed on the MH sample than those of the M sample are due to the reduction of the pre-existing surface films formed after mechanical grinding during the H_2 annealing treatment. The low estimated equivalent thickness of the inner layer of the MH sample (0.3 nm) is consistent with a less homogeneously thick and possibly discontinuous inner layer proposed by the ToF-SIMS results. The inner Cr(III) oxide would be locally thick due to a preferential local supply of Cr metal during nucleation and the initial growth of the oxide film formed by surface reoxidation. Between these local areas, the Cr(III) oxide would be thinner or even not have been formed, weakening the corrosion protection provided by the inner barrier layer. Regarding the composition of the outer layer, it is more enriched in Cr(III) hydroxide after reoxidation than in the pre-existing native surface film, in agreement with the ToF-SIMS results, indicating a more pronounced selective oxidation of Cr during surface reoxidation. The estimated composition of the modified alloy under the surface film shows significant Cr depletion for both surface preparation methods (15 and 13 at.% Cr for M and MH, respectively) compared to the nominal bulk composition of the alloy (20 at.% Cr). A slightly more pronounced Cr depletion of the modified alloy substrate for the MH sample is consistent with the more pronounced selective oxidation of Cr during reoxidation. It may be attributed to the lower free energy of formation for Cr oxide and Cr hydroxide than for Ni hydroxide [60, 61, 62], combined with the effect of wet oxidation of the cold-worked surface during the initial formation of the native surface film versus dry oxidation of the recrystallized surface during the reformation of the native surface film. It is shown that

the Ni(II) hydroxide and Cr(III) (hydr)oxide species natively formed on the alloy cold-worked surface after mechanical grinding are reduced at high temperature during the H_2 annealing treatment. Most likely, the bare recrystallized metallic alloy surface is exposed to reoxidation during quenching and/or sample transfer during which Cr oxidation is more selective than after mechanical grinding. In this case, the oxide growth at saturation is more limited in thickness, resulting in a less homogeneous protection provided by the inner Cr(III) oxide layer.

Table 1. Thickness and composition of the native surface films formed on the M and MH surfaces estimated from the XPS decomposition results using a bilayer model assuming an inner layer of 100% Cr_2O_3 and a mixed outer layer of $Ni(OH)_2$ + $Cr(OH)_3$.

Preparation	Layer	Thickness / nm	Relative composition / %		Alloy composition under surface film / %	
M	Total	0.8	Ni-O/-OH	Cr-O/-OH	Ni	Cr
			-	-	85	15
	Outer	0.3	$Ni(OH)_2$	$Cr(OH)_3$	-	
			66	34		
	Inner	0.5	Cr_2O_3			
			100			
MH	Total	0.5	Ni-O/-OH	Cr-O/-OH	Ni	Cr
			-	-	87	13
	Outer	0.2	$Ni(OH)_2$	$Cr(OH)_3$	-	
			26	74		
	Inner	0.3	Cr_2O_3			
			100			

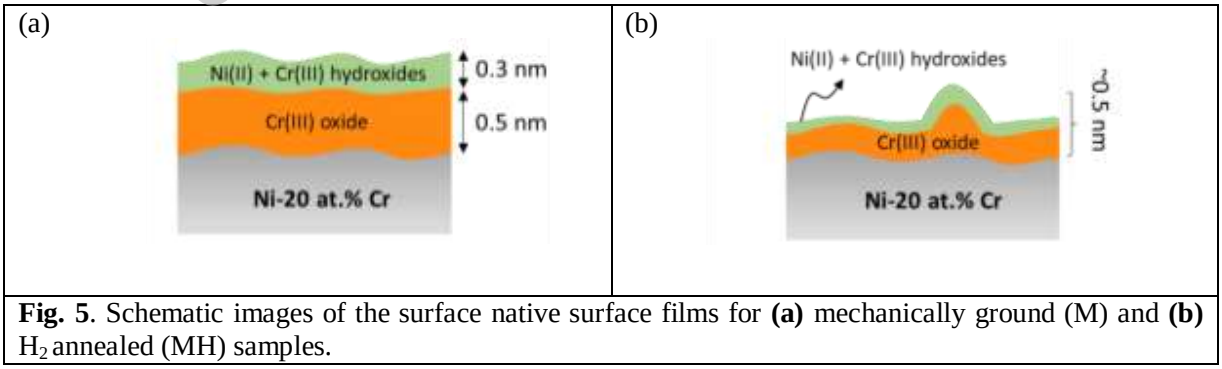

Fig. 5. Schematic images of the surface native surface films for **(a)** mechanically ground (M) and **(b)** H_2 annealed (MH) samples.

Electrochemical responses

The electrochemical reactivity of the surfaces prepared by the M and MH methods was investigated *via* LSV and potentiostatic experiments performed in a 0.5 M H_2SO_4 solution (**Fig. 6**). The LSV curves in **Fig. 6(a)** show that the MH surface is more active in that the potential at j = 0 ($E_{j=0}$ = -0.26 V vs. SCE) is more negative than for the M sample ($E_{j=0}$ = -0.18 V vs. SCE), consistent with open circuit potential (E_{oc}) values of -0.24 V and -0.13 V vs. SCE for the MH and M samples, respectively (not shown here).

An obvious active current density peak ($E_{j=0}$ < E < 0.15 V vs. SCE) is monitored for the MH whereas no clear peak is observed for the M. This active peak may be again attributed to less homogeneous inner Cr-rich inner barrier layer formed during reoxidation after the H_2 annealing. For E > 0.15 V vs. SCE, a well-defined passive potential domain is observed for both surface preparations with an almost potential independent current density at 5 ~ 7 µA cm^{-2}. The current density responses in the passive (0.15 V < E < 0.82 V vs. SCE) and transpassive domains (E > 0.82 V vs. SCE) are nearly superimposable for the two cases.

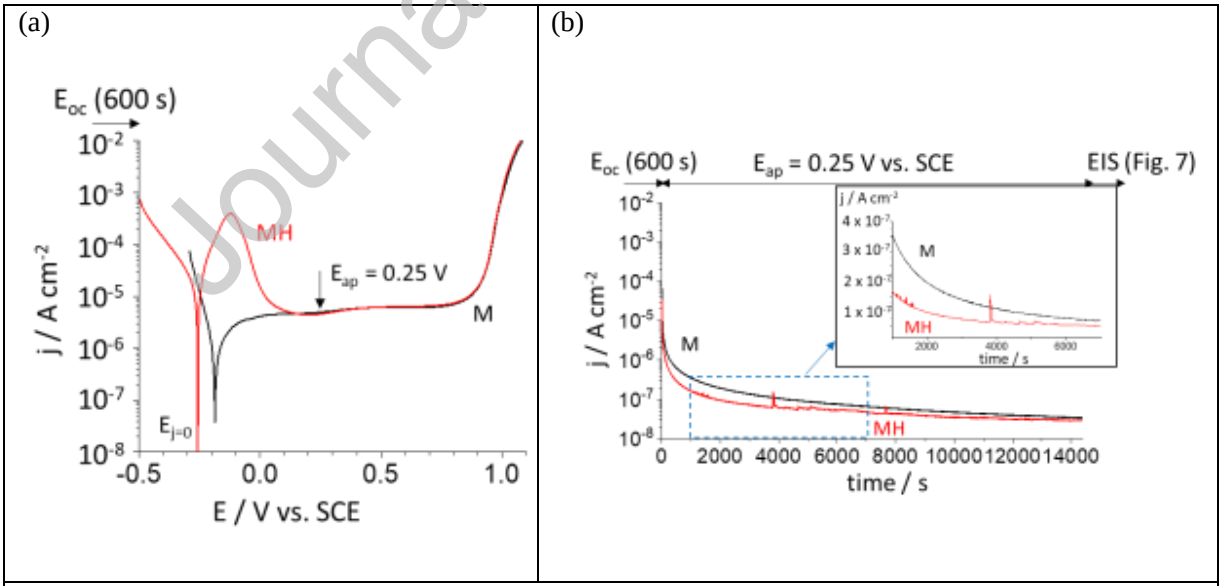

Fig. 6. Electrochemical responses of the mechanically ground (M), and H_2 annealed (MH) samples. **(a)** LSV with 1 mV s^{-1} scan rate; **(b)** current density decay as a function of time at a constant passivation potential of 0.25 V vs. SCE in 0.5 M H_2SO_4.

A potential of 0.25 V vs. SCE in the passive potential domain of **Fig. 6(a)** was chosen to investigate the electrochemical passivation of each surface preparation method. The experiments were conducted as follows; 1) an open circuit measurement was conducted for 600 s; 2) then a constant potential of 0.25 V vs. SCE was applied for 4 h; 3) followed by a potentiostatic EIS measurement at the same potential. **Fig. 6(b)** shows the current density responses during the potentiostatic experiments. Both samples show typical current decays at constant potential indicating passive film formation and film growth by lowering the potential across the oxide/metal interface [63]. In the MH case, the passive current density is lower than in the M case, indicating the formation of a more corrosion resistant passive film formation for the H_2 annealed surface [20, 64, 65]. A certain degree of instability is however observed for the MH case with anodic current density spikes shown before reaching a quasi-steady state, as shown in the inset in **Fig. 6(b)**.

The potentiostatic EIS measurements were performed following 4 h of potentiostatic hold at the same potential. The Nyquist plots are shown in **Fig. 7(a)** with an equivalent circuit used to fit the data presented in the inset, and the fitting results are provided in **Table 2**. The CPE_1/R_1 and CPE_2/R_2 represent the outer and inner layer components in the passive films, respectively [66, 67]. The CPE_{ct}/R_{ct} represents the charge-transfer impedance, and CPE_{dl} is the double layer component. The R_e corrected Bode modulus and phase plots are shown in **Figs. 7(b)** and **7(c)**, respectively. The CPE is well defined in a relatively wide frequency domain for $10^{-1} < f < 10^5$ Hz where the R_e corrected phase shift was nearly -80° (**Fig. 7(c))**, justifying the use of CPE parameters to estimate interfacial properties. Neglecting the $1/R_{ct}$ term in **Eq. 1** is also justified by the fitting results where R_{ct} (~10^6 Ω cm^2) >> R_e (~3 Ω cm^2). For both M and MH surfaces, the inner layer would be more stable than the outer layer since R_2 (5.1 x 10^5 and 1.1 x 10^6 Ω cm^2 for M and MH, respectively) are higher than R_1 (1.3 x 10^5 and 6.2 x 10^2 Ω cm^2 for M and MH, respectively). For the MH sample, a much larger difference between the inner and outer layer resistance (1.1 x 10^6 and 6.2 x 10^2 Ω cm^2, respectively) is estimated than for the M sample (5.1 x 10^5 and 1.3 x 10^5

Ω cm^2, respectively). The thickness of the passive film (δ) was calculated by **Eq. 4** using the CPE parameters, and the corrected C_δ taking into account C_{dl} and R_e as described in the experimental section. A relative dielectric constant of the passive film (ε_{rel} = 11) was used with average dielectric constant values of the oxidized Cr and Ni species previously reported for Ni- and Cr-containing alloys [68, 69]. The estimated δ values are 1.1 and 1.0 nm for the M and MH samples, respectively, which shows close agreement with the values obtained from XPS analysis discussed in the following section.

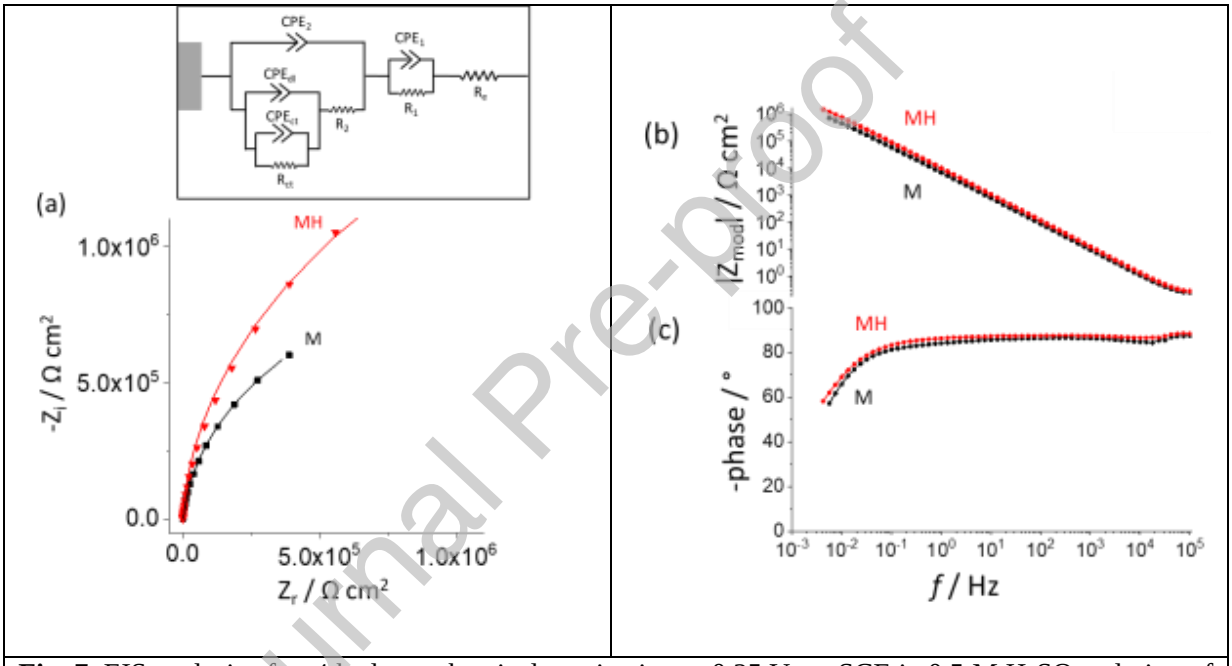

Fig. 7. EIS analysis after 4 h electrochemical passivation at 0.25 V vs. SCE in 0.5 M H_2SO_4 solution of the mechanically ground (M) and the H_2 annealed (MH) samples; **(a)** Nyquist, **(b)** Bode magnitude, and **(c)** Bode phase plots. The equivalent circuit used to fit the EIS spectra is given in the inset of **Fig. 7(a)**. Symbols represent the recorded data points and solid lines represent the fitting results.

Table 2. EIS fitting results for the samples M and MH during potentiostatic EIS at 0.25 V vs. SCE in 0.5 M H_2SO_4. The equivalent circuit used for fitting is provided in the inset of **Fig. 7(a)**.

	M	MH
R_1 / Ω cm^2	1.3 x 10^5	6.2 x 10^2
Q_1 / F s$^{\alpha-1}$ cm^{-2}	125 x 10^{-6}	700 x 10^{-6}

α_1	0.95	0.84
R_2 / Ω cm^2	5.1 x 10^5	1.1 x 10^6
Q_2 / F $s^{\alpha-1}$ cm^{-2}	32 x 10^{-6}	17 x 10^{-6}
α_2	0.95	0.98
Q_{dl} / F $s^{\alpha-1}$ cm^{-2}	5.2 x 10^{-6}	1.3 x 10^{-6}
α_{dl}	0.99	0.90
Q_{ct}	0.15 x 10^{-6}	2.6 x 10^{-6}
α_{ct}	0.95	0.70
R_{ct} / Ω cm^2	9.6 x 10^5	2.3 x 10^6
R_e / Ω cm^2	3.5	3.1
δ / nm	1.1	1.0
ρ_δ / Ω cm	1.5 x 10^5	2.5 x 10^4

ToF-SIMS depth profile after electrochemical passivation

Fig. 8 shows the ToF-SIMS depth profiles obtained after electrochemical passivation of each sample at 0.25 V vs. SCE in 0.5 M H_2SO_4 for 4 h. A bilayer passive film formation is indicated by a sequence of the selected ion intensity peaks, similar to that observed prior to electrochemical passivation **(Fig. 1**). The signal decay times for characteristic ions of the oxidized species are much longer after (**Fig. 8**) than before (**Fig. 1**) passivation, suggesting an increased roughness [19, 58] of the electrochemically passivated surfaces. For the MH case after electrochemical passivation, a relatively less homogeneously thick inner layer formation is indicated by a large pseudo Ni_2^- plateau (10 s < t < 30 s, **Fig. 8(b)** [19, 58]. Note that the same but narrower type of Ni_2^- plateau (5 s < t < 15 s) was observed for the MH surface before electrochemical passivation (**Fig. 1(b)**). In **Fig. 8**, the $CrO_3H_2^-$ profile (related to Cr(III) hydroxide species) obtained after electrochemical passivation is more intense than the $NiO_2H_2^-$ profile (related to Ni(II) hydroxide species). This opposite trend to that observed before passivation (**Fig. 1**) is supported by the XPS analysis presented in the next section. Cr(III) hydroxide species enrichment during

electrochemical passivation for both M and MH surfaces results from selective dissolution of the Ni(II) hydroxide species [32]. This enrichment would more likely occur at the interface between inner and outer layers ($CrO_3H_2^-/NiO_2H_2^-$ intensity ratio of 4.5 and 1.6 for M and MH, respectively) as indicated by the slower decay of the $CrO_3H_2^-$ signal compared to that of the $NiO_2H_2^-$ signal at this interface for both cases shown in **Fig 8**.

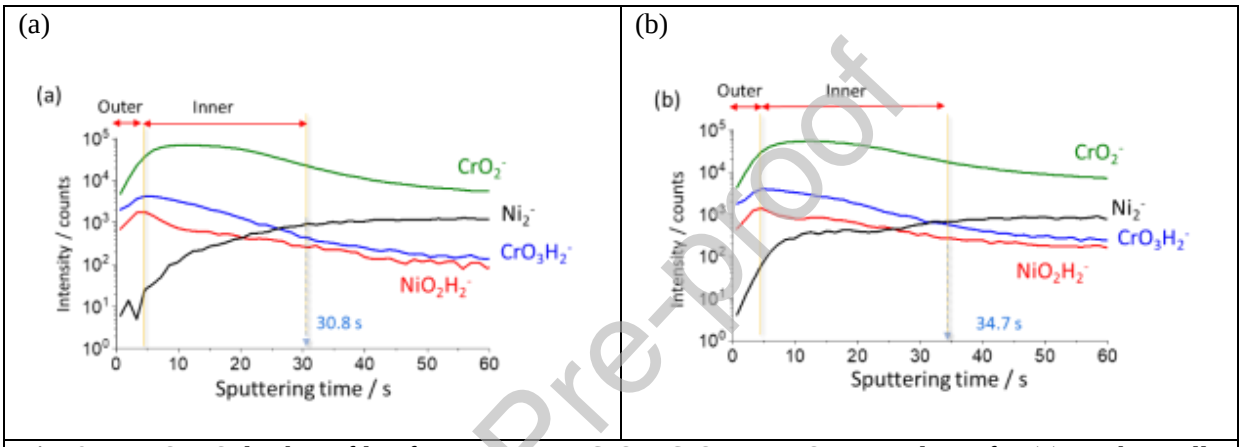

Fig. 8. ToF-SIMS depth profile of negative ions CrO_2^-, $CrO_3H_2^-$, $NiO_2H_2^-$, and Ni_2^- for **(a)** mechanically ground (M) and **(b)** H_2 annealed (MH) samples after potentiostatic passivation for 4 h at 0.25 V vs. SCE in 0.5 M H_2SO_4.

High-resolution XPS analysis after electrochemical passivation

The high-resolution Cr 2p, Ni $2p_{3/2}$, and O 1s core level XPS spectra recorded after electrochemical passivation of the M and MH surfaces at 0.25 V vs. SCE in 0.5 M H_2SO_4 for 4 h are shown in **Figs. 9**, **10** and **11**, respectively. The Cr 2p spectra presented in **Fig. 9** show increased Cr(III) hydroxide formation during electrochemical passivation of both surfaces, as indicated by the increased relative intensity of the Cr(III) hydroxide peak compared to the surfaces prior to electrochemical passivation (**Fig. 1**). This is in agreement with previous observations of similar systems [70, 71], and consistent with the selective dissolution of Ni(II) hydroxide species. Based on the ToF-SIMS result in **Fig. 8**, it is reasonable to conclude that the Cr(III) hydroxide species would be more concentrated near the

inner/outer layer interface. From the XPS results, the Cr(III) hydroxide enrichment is more pronounced for the electrochemically passivated MH surface (**Fig. 9(b)**) than for the M surface (**Fig. 9(a)**). **Figs. 10** and **11** show that similar Ni and O surface species were observed after the electrochemical passivation compared to the case before passivation.

A bilayer model is applied to estimate the equivalent thickness and composition of the passive films and the modified composition of the underlying alloy for the electrochemically passivated samples. Again, the results presented in **Table 3** must be considered with caution due to the inhomogeneity in thickness of the passive film formed on the MH sample suggested by the ToF-SIMS results. It can provide a basis for comparing the M and MH surfaces shown schematically in **Fig. 12**. After electrochemical passivation, an equivalent inner layer passive film thickness of 0.5 nm is calculated for the M sample similar to the case before passivation. A slightly thinner Cr(III) oxide inner layer of 0.4 nm is estimated for the MH sample. The equivalent thickness values of the outer hydroxide layer are 0.4 nm and 0.6 nm for the passivated M and MH surfaces, respectively. In the outer layer, the relative composition of Cr(III) to Ni(II) hydroxides increases after electrochemical passivation (70% and 92% for M and MH respectively, in **Table 3**) compared to before passivation (34% and 74% for M and MH respectively, in **Table 1**). This indicates an increased formation of Cr(III) hydroxide species due to the selective dissolution of Ni(II) hydroxide species during electrochemical passivation, in agreement with ToF-SIMS results. The Cr(III) enrichment in the outer layer is more pronounced for the MH surface (92%) than for the M surface (70%), which may account for the high oxidation peak in the active/passive transition domain in the LSV result for the MH sample. The overall passive film thickness values are estimated to be 0.9 and 1.0 nm for the passivated M and MH surfaces, respectively, in close agreement with EIS analysis (1.1 nm and 1.0 nm, respectively).

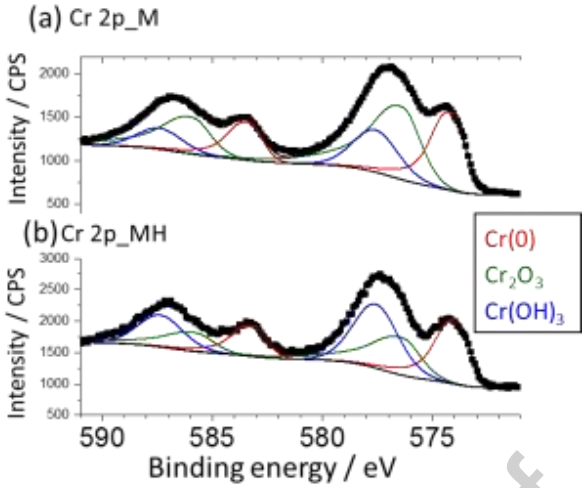

Fig. 9. High-resolution XPS Cr 2p spectra for **(a)** mechanically ground (M) and **(b)** H_2 annealed (MH) samples after potentiostatic passivation for 4 h at 0.25 V vs. SCE in 0.5 M H_2SO_4.

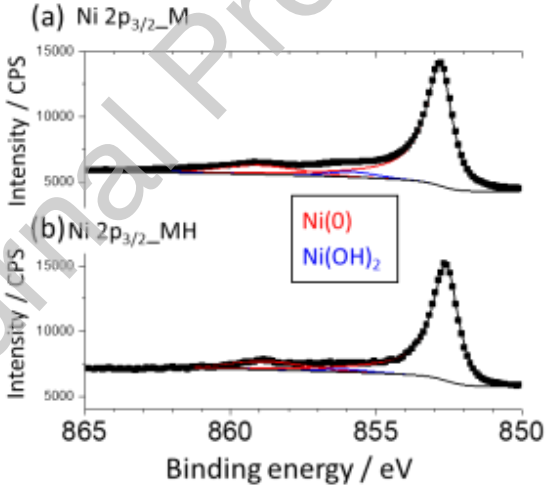

Fig. 10. High-resolution XPS Ni $2p_{3/2}$ spectra for **(a)** mechanically ground (M) and **(b)** H_2 annealed (MH) samples after potentiostatic passivation for 4 h at 0.25 V vs. SCE in 0.5 M H_2SO_4.

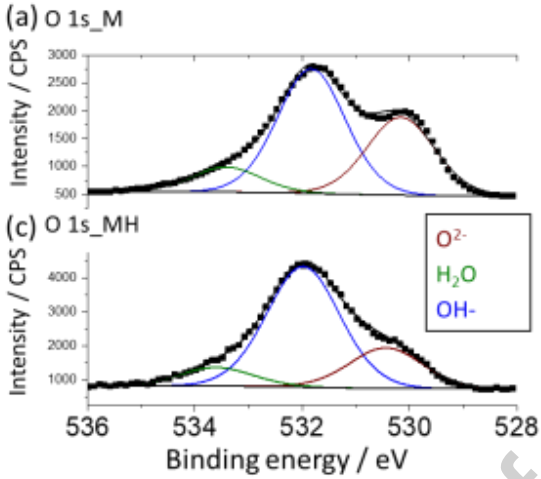

Fig. 11. High-resolution XPS O 1s spectra for **(a)** mechanically ground (M) and **(b)** H_2 annealed (MH) samples after potentiostatic passivation for 4 h at 0.25 V vs. SCE in 0.5 M H_2SO_4.

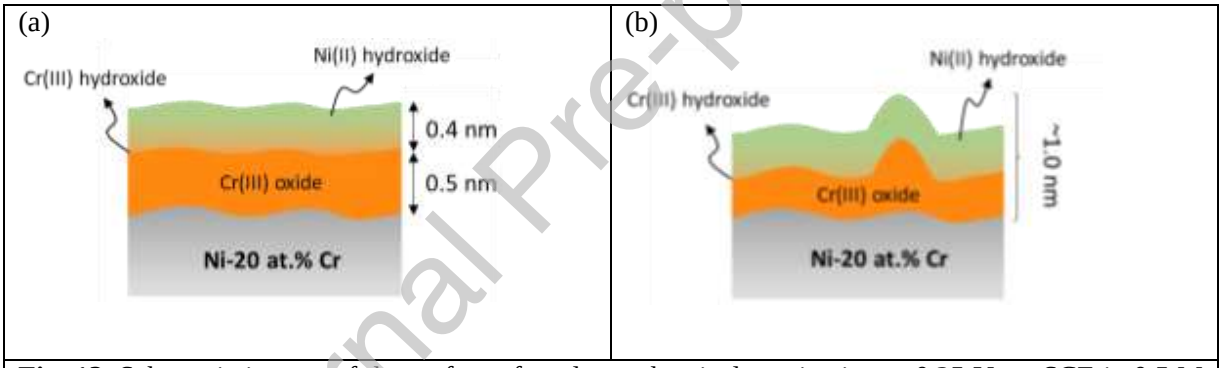

Fig. 12. Schematic images of the surface after electrochemical passivation at 0.25 V vs. SCE in 0.5 M H_2SO_4 for 4 h of the **(a)** mechanically ground (M) and **(b)** H_2 annealed (MH) surfaces.

Table 3. Thickness and composition of the passive films formed on the M and MH surfaces after 4 h of potentiostatic hold experiments at 0.25 V vs. SCE in 0.5 M H_2SO_4 calculated from the XPS decomposition results using a bilayer model assuming an inner layer of 100% Cr_2O_3 and a mixed outer layer of $Ni(OH)_2$ + $Cr(OH)_3$.

Preparation	Layer	Thickness / nm	Relative composition / %		Alloy composition under surface film / %	
M	Total	0.9	Ni-O/-OH	Cr-O/-OH	Ni	Cr
			-	-	83	17
	Outer	0.4	$Ni(OH)_2$	$Cr(OH)_3$	-	
			30	70		
	Inner	0.5	Cr_2O_3			
			100			
MH	Total	1.0	Ni-O/-OH	Cr-O/-OH	Ni	Cr

			-	-	84	16
	Outer	0.6	$Ni(OH)_2$	$Cr(OH)_3$	-	
			8	92		
	Inner	0.4	Cr_2O_3			
			100			

Discussion

In this work, the effect of H_2 annealing at T = 800°C on the surface chemical state and electrochemical passivation of a polycrystalline Ni-20 at.% Cr alloy was investigated. The native duplex oxide/hydroxide surface film formed on the cold-worked surface remaining from mechanical grinding was reduced by the H_2 annealing treatment, as indicated by the ToF-SIMS depth profile (**Fig. 1**) and the XPS high-resolution spectral analysis (**Figs. 2-4**). The H_2 annealed surface reoxidizes during quenching due to the oxygen/water vapor present in the H_2 gas stream and/or during sample transfer to air. Thus, a new duplex oxide/hydroxide surface film forms on the recrystallized surface. On both as-prepared surfaces, the inner layer is mainly of Cr(III) oxide and the outer layer is a mixture of Cr(III) and Ni(II) hydroxides. The inner layer of the native surface film grown on the recrystallized alloy surface is non-uniform in thickness, as suggested by Tof-SIMS depth profiling and reflected by the low value (0.3 nm) of the equivalent thickness estimated from XPS analysis.

An obvious difference between the two surface preparation methods is in the active potential domain during the LSV experiment in 0.5 M H_2SO_4 (**Fig. 6(a)**). An active current density peak is observed for the MH case while no active peak is monitored for the M case in this potential domain. Despite this high active current peak in the active/passive transition in the LSV, the MH sample shows a slightly lower current density than the M sample during potentiostatic hold experiment at 0.25 V vs. SCE (**Fig. 6(b)**), an indication of a stable passive film formation. However, more passivity breakdown events are observed during the electrochemical passivation of the H_2 annealed surface, suggesting a slightly higher instability during the passive film formation before reaching a quasi-steady state [72]. Potentiostatic EIS at the same potential showed higher inner layer resistance for the H_2 annealed surface

(1.1×10^6 Ω cm^2) than for the mechanically ground surface (5.1×10^5 Ω cm^2) (**Fig. 7, Table 2**), indicating the formation of a more protective Cr(III)-based inner barrier layer film formation on the H_2 annealed surface during electrochemical passivation. ToF-SIMS (**Fig. 8**) and XPS (**Figs. 9 - 11**) analysis of the electrochemically passivated surfaces show enhanced Cr(III) hydroxide formation for both surface preparation methods. For the H_2 annealed surface, the relative content of the outer Cr(III) hydroxide layer is 92% and 70% for the mechanically ground surface (**Table 3)**.

These observations derived from *in situ* electrochemical and *ex situ* surface characterizations suggest the following mechanisms of passive film formation. On the mechanically ground surface, a relatively uniform native surface film is formed with an inner layer of Cr(III) oxide and an outer layer of mixed Cr(III) and Ni(II) hydroxides. On the H_2 annealed sample, the surface layer formed after mechanical grinding is reduced during the high-temperature H_2 annealing. A new duplex surface layer is reformed during the post-annealing sample transfer process in air with a less protective inner layer of inhomogeneous thickness (**Fig. 5(b)**). This less stable surface film formed after the H_2 annealing treatment readily oxidizes when in contact with H_2SO_4, resulting in an active oxidation peak in the LSV curve (**Fig. 6(a)**). The activated area where the inner layer would initially be thinner may undergo the selective dissolution of Ni leading to an enrichment in Cr(III) oxide and hydroxide species during electrochemical passivation (**Fig. 12(b)**). The non-activated area (**Fig. 12(b)**) where the inner layer would initially be thicker and more protective is not significantly modified by the selective Ni dissolution during electrochemical passivation. The enhanced overall corrosion resistance of the passive film formed on the MH sample may be explained as follows. The recrystallized surface of the H_2 annealed sample is less homogeneously covered and less well protected by the native surface film than the cold-worked surface of the non-annealed sample. The weaker sites of the H_2 annealed sample, activated by the electrochemical polarization, are ultimately well protected by the electrochemically formed passive film. Cr enrichment is favored by the selective Ni dissolution in these initially weaker (less well protected) sites.

Increased Cr(III) hydroxide formation in the outer layer may be responsible for the passivity breakdown events observed during potentiostatic passivation of the MH sample (**Fig. 6(b)**). The formation of a less corrosion resistant Cr hydroxide outer layer by consuming a more corrosion resistant Cr oxide inner layer has been documented previously [64, 73, 74]. In the present work, the resistivity between the outer layer and the electrolyte, ρ_δ, was calculated using the power-law model [75] from the EIS spectra as:

$$\rho_\delta = [(\varepsilon_{rel}\,\varepsilon_0)^\alpha / (g\,\delta\,Q)]^{1/(1-\alpha)} \quad [5]$$

$$g = 1 + 2.88(1-\alpha)^{2.375} \quad [6]$$

assuming a resistivity distribution in the passive film. The passive film thickness, δ, was taken from XPS analysis after passivation (**Table 3**), and the CPE parameters (Q and α) were obtained from the graphical analysis of the EIS spectra [54] as described in the experimental section. The ρ_δ value obtained for the H_2 annealed surface after passivation (2.5×10^4 Ω cm) was one order of magnitude lower than that for the mechanically ground surface after passivation (1.5×10^5 Ω cm), which may also be attributed to a higher Cr hydroxide content at the outer surface for the H_2 annealed surface. The ρ_δ values obtained in this work agree with the ρ_δ profile analysis in the passive film of a Ni-20Cr alloy in various pH solutions [76]. It should be noted that this analysis may be limited in a qualitative level as the power-law model calculation assumes that the dielectric constant is independent of position within the passive film whereas a bilayer passive film was monitored by *ex situ* characterization in the present work. Therefore, it is possible that the dielectric constants in the inner and outer layer are significantly different, resulting in a less accurate ρ_δ calculation, although this assumption of a uniform dielectric constant may not be critical if the CPE results from a dielectric response of the material shows a normal distribution of time constants [77].

Conclusions

- Surface preparation by mechanical grinding or subsequent high-temperature H_2 annealing of the Ni-20 at.% Cr alloy results in a duplex surface film formation with an inner layer consisting mainly of Cr(III) oxide and an outer layer of mixed Cr(III) and Ni(II) hydroxides.
- On the H_2 annealed surface, less Cr(III), Ni(II) hydroxides, and less Cr(III) oxide species were observed indicating that the native surface film initially formed on the cold-worked surface after mechanical grinding is effectively reduced during the annealing, then regrown by reoxidation during quenching and/or transfer to ambient air. The newly formed native surface film is overall thinner with a relatively less homogeneous thickness and a less protective inner barrier layer.
- An active current peak during the potentiodynamic polarization experiment observed for the H_2 annealed sample is attributed to the oxidation of the weaker sites of the inner barrier layer of non-homogeneous thickness when exposed to H_2SO_4.
- A passive film formation with better corrosion resistance for the H_2 annealed sample than the mechanically ground sample is indicated by electrochemical measurements. A lower passive current density is monitored for the H_2 annealed sample during potentiostatic hold experiment at 0.25 V vs. SCE in 0.5 M H_2SO_4. A higher passive film resistance as well as charge transfer resistance for the H_2 annealed sample is estimated by equivalent circuit fitting of the EIS analysis.
- A bilayer surface film is characterized after electrochemical passivation of the H_2 annealed surface, with a higher resistance of the inner layer than for the mechanically ground surface. The enhanced corrosion resistance of the H_2 annealed sample surface is attributed to the formation of a more protective inner Cr(III) oxide barrier layer caused by the selective Ni dissolution and associated Cr enrichment, providing corrosion resistance to initially weakly protected sites.

CRediT authorship contribution statement

J.H.: Conceptualization, Methodology, Investigation, Formal analysis, Data Curation, Writing – Original Draft, Writing – Review & Editing, **S.N.**: Investigation, Data Curation, **L.W.**: Investigation, Data Curation, **A.S.**: Investigation, Formal analysis, Writing – Review & Editing, **L.K.**: Investigation, **S.Z.**: Investigation, Formal analysis, Data Curation, Writing – Review & Editing, **D.M.**: Conceptualization, Methodology, Writing – Review & Editing, **V.M.**: Validation, Writing – Review & Editing, **P.M.**: Conceptualization, Methodology, Supervision, Writing – Review & Editing, Project administration, Funding acquisition.

Acknowledgments

The research was funded by the Office of Naval Research Global (ONRG) under grant #N62909-18-1-2172. The ToF-SIMS instrument was partially funded by Région île-de-France. Authors would like to thank Dr. Zuocheng Wang for preliminary experiments.

Figure captions and Tables

Fig. 1. ToF-SIMS depth profiles of negative ions CrO_2^-, $CrO_3H_2^-$, $NiO_2H_2^-$, and Ni_2^- for **(a)** mechanically ground (M) and **(b)** H_2 annealed (MH) samples.

Fig. 2. High-resolution XPS Cr 2p core level spectra for **(a)** mechanically ground (M) and **(b)** H_2 annealed (MH) samples.

Fig. 3. High-resolution XPS Ni $2p_{3/2}$ core level spectra for **(a)** mechanically ground (M) and **(b)** H_2 annealed (MH) samples.

Fig. 4. High-resolution XPS O 1s core level spectra for **(a)** mechanically ground (M) and **(b)** H_2 annealed (MH) samples.

Fig. 5. Schematic images of the surface native surface films for **(a)** mechanically ground (M) and **(b)** H_2 annealed (MH) samples.

Fig. 6. Electrochemical responses of the mechanically ground (M), and H_2 annealed (MH) samples. **(a)** LSV with 1 mV s^{-1} scan rate; **(b)** current density decay as a function of time at a constant passivation potential of 0.25 V vs. SCE in 0.5 M H_2SO_4.

Fig. 7. EIS analysis after 4 h electrochemical passivation at 0.25 V vs. SCE in 0.5 M H_2SO_4 solution of the mechanically ground (M) and the H_2 annealed (MH) samples; **(a)** Nyquist, **(b)** Bode magnitude, and **(c)** Bode phase plots. The equivalent circuit used to fit the EIS spectra is given in the inset of **Fig. 7(a)**. Symbols represent the recorded data points and solid lines represent the fitting results.

Fig. 8. ToF-SIMS depth profile of negative ions CrO_2^-, $CrO_3H_2^-$, $NiO_2H_2^-$, and Ni_2^- for **(a)** mechanically ground (M) and **(b)** H_2 annealed (MH) samples after potentiostatic passivation for 4 h at 0.25 V vs. SCE in 0.5 M H_2SO_4.

Fig. 9. High-resolution XPS Cr 2p spectra for **(a)** mechanically ground (M) and **(b)** H_2 annealed (MH) samples after potentiostatic passivation for 4 h at 0.25 V vs. SCE in 0.5 M H_2SO_4.

Fig. 10. High-resolution XPS Ni $2p_{3/2}$ spectra for **(a)** mechanically ground (M) and **(b)** H_2 annealed (MH) samples after potentiostatic passivation for 4 h at 0.25 V vs. SCE in 0.5 M H_2SO_4.

Fig. 11. High-resolution XPS O 1s spectra for **(a)** mechanically ground (M) and **(b)** H_2 annealed (MH) samples after potentiostatic passivation for 4 h at 0.25 V vs. SCE in 0.5 M H_2SO_4.

Fig. 12. Schematic images of the surface after electrochemical passivation at 0.25 V vs. SCE in 0.5 M H_2SO_4 for 4 h of the **(a)** mechanically ground (M) and **(b)** H_2 annealed (MH) surfaces.

Table 1. Thickness and composition of the native surface films formed on the M and MH surfaces estimated from the XPS decomposition results using a bilayer model assuming an inner layer of 100% Cr_2O_3 and a mixed outer layer of $Ni(OH)_2$ + $Cr(OH)_3$.

Table 2. EIS fitting results for the samples M and MH during potentiostatic EIS at 0.25 V vs. SCE in 0.5 M H_2SO_4. The equivalent circuit used for fitting is provided in the inset of **Fig. 7(a)**.

Table 3. Thickness and composition of the passive films formed on the M and MH surfaces after 4 h of potentiostatic hold experiments at 0.25 V vs. SCE in 0.5 M H_2SO_4 calculated from the XPS decomposition results using a bilayer model assuming an inner layer of 100% Cr_2O_3 and a mixed outer layer of $Ni(OH)_2$ + $Cr(OH)_3$.

References

CRediT authorship contribution statement

J.H.: Conceptualization, Methodology, Investigation, Formal analysis, Data Curation, Writing – Original Draft, Writing – Review & Editing, **S.N.**: Investigation, Data Curation, **L.W.**: Investigation, Data Curation, **A.S.**: Investigation, Formal analysis, Writing – Review & Editing, **L.K.**: Investigation, **S.Z.**: Investigation, Formal analysis, Data Curation, Writing – Review & Editing, **D.M.**: Conceptualization, Methodology, Writing – Review & Editing, **V.M.**: Validation, Writing – Review & Editing, **P.M.**: Conceptualization, Methodology, Supervision, Writing – Review & Editing, Project administration, Funding acquisition.

Declaration of interests

☒The authors declare that they have no known competing financial interests or personal relationships that could have appeared to influence the work reported in this paper.

☐The authors declare the following financial interests/personal relationships which may be considered as potential competing interests:

[1] K. Rokosz, G. Solecki, G. Mori, R. Fluch, M. Kapp, and J. Lahtinen, "Effect of polishing on electrochemical behavior and passive layer composition of different stainless steels", *Materials*, **13**, 3402 (2020). https://doi.org/10.3390/ma13153402
[2] M.J. Sohrabi, H. Mirzadeh, and C. Dehghanian, "Unraveling the effects of surface preparation on the pitting corrosion resistance of austenitic stainless steel", *Archi. Civil & Mech. Engin.*, **20**:8 (2020). https://doi.org/10.1007/s43452-020-0010-z
[3] J.R. Davis, "Nickel, Cobalt, and their alloys", ASM international, p293-297 (2000).
[4] N.S. McIntyre, L. Kover, and T.C. Chan, "Studies of initial oxidation of nickel-chromium alloys: Surface annealing by hydrogen ion bombardment", *J. Vacuum Sci. & Tech.* A, **4**, 1866 (1986). https://doi.org/10.1116/1.573737
[5] K. Jaffré, B. Ter-Ovanessian, H. Abe, N. Mary, B. Normand, and Y. Watanabe, "Effect of mechanical surface treatments on the surface state and passive behavior of 304L stainless steel", *Metals*, **11**, 135 (2021). https://doi.org/10.3390/met11010135
[6] M. Scendo, W. Zorawski, K. Staszewska-Samson, M. Makrenek, and A. Goral, "Influence of surface pretreatment on the corrosion resistance of cold-sprayed nickel coatings in acidic chloride solution", *J. Mat. Eng. & Perf.*, **27**, 1725-1737 (2018). https://doi.org/10.1007/s11665-018-3298-6
[7] D. Serafin, W.J. Nowak, and B. Wierzba, "Differences in oxides morphology as a result of surface preparation of NiFe alloy", *Surf. & Coat. Tech.*, **385**(15), 125421 (2020). https://doi.org/10.1016/j.surfcoat.2020.125421
[8] N. Haghdadi, M. Laleh, M. Moyle, and S. Primig, "Additive manufacturing of steels: a review of achievements and challenges", *J. Mater. Sci.*, **56**, 64–107 (2021). https://doi.org/10.1007/s10853-020-05109-0
[9] J. Han and O. Gharbi, "Current state of electrochemical techniques and corrosion rate analysis for next-generation materials", *Current Opinion in Electrochemistry*, **36**, 101131. https://doi.org/10.1016/j.coelec.2022.101131
[10] M.A. Melia, J.G. Duran, J.R. Koepke, D.J. Saiz, B.H. Jared, and E.J. Schindelholz, "How build angle and post-processing impact roughness and corrosion of additively manufactured 316L stainless steel", *npj Mat. Degrad.*, **4**, 21 (2020). https://doi.org/10.1038/s41529-020-00126-5

[11] L. Ma, F. Wiame, V. Maurice, and P. Marcus "Origin of nanoscale heterogeneity in the surface oxide film protecting stainless steel against corrosion", *npj Mat. Degrad.*, **3**, 29 (2019). https://doi.org/10.1038/s41529-019-0091-4
[12] Z. Wang, E-.M. Paschalidou, A. Seyeux, S. Zanna, V. Maurice, and P. Marcus, "Mechanisms of Cr and Mo enrichments in the passive oxide film on 316L austenitic stainless steel", *Front. Mater.*, **6**:232 (2019). https://doi.org/10.3389/fmats.2019.00232
[13] I. Olefjord, "The passive state of stainless steels", *Mat. Sci., & Eng.*, **42**, 161 (1980). https://doi.org/10.1016/0025-5416(80)90025-7
[14] P. Keller, and H-.-H. Strehblow, "XPS investigations of electrochemically formed passive layers on Fe/Cr-alloys in 0.5 M H_2SO_4", *Corros. Sci.*, **46**(8), 1939-1952 (2004). https://doi.org/10.1016/j.corsci.2004.01.007
[15] W.H. Blades, and P. Reinke, "From alloy to oxide: Capturing the early stages of oxidation on Ni-Cr(100) alloys", *ACS Appl. Mater. Interfaces*, **10**, 43219-43229 (2018). https://doi.org/10.1021/acsami.8b15210
[16] X. Li, and K. Ogle, "The passivation of Ni-Cr-Mo alloys: Time resolved enrichment and dissolution of Cr and Mo during passive-active cycles", *J. Electrochem. Soc.*, **166**(11), C3179-C3185 (2019). https://doi.org/10.1149/2.0201911jes
[17] L. Luo, L. Zou, D.K. Schreiber, M.J. Olszta, D.R. Baer, S.M. Bruemmer, G. Zhou, and C.-M. Wang, "In situ atomic scale visualization of surface kinetics driven dynamics of oxide growth on Ni-Cr surface", *Chem. Commu.*, **52**, 3300 (2016). https://doi.org/10.1039/c5cc09165a
[18] D.K. Schreiber, M.J. Olszta, and S.M. Bruemmer, "Grain boundary depletion and migration during selective oxidation of Cr in a Ni-5Cr binary alloy exposed to high-temperature hydrogenated water", *Scripta Mat.*, **89**, 41-44 (2014). https://doi.org/10.1016/j.scriptamat.2014.06.022
[19] Z. Wang, C. Carrière, A. Seyeux, S. Zanna, D. Mercier, and P. Marcus, "Thermal stability of surface oxide on nickel alloys (NiCr and NiCrMo) investigated by XPs and ToF-SIMS", *Appl. Surf. Sci.*, **576**, 151836 (2022). https://doi.org/10.1016/j.apsusc.2021.151836
[20] V. Maurice, W.P. Yang, and P. Marcus, "XPS and STM study of passive films formed on Fe-22Cr(110) single-crystal surfaces", *J. Electrochem. Soc.*, **143**(4), 1182 (1996). https://doi.org/10.1149/1.1836616
[21] V. Maurice, W.P. Yang, and P. Marcus, "X-ray photoelectron spectroscopy and scanning tunneling microscopy study of passive films formed on (100) Fe-18Cr-13Ni single-crystal surface, *J. Electrochem. Soc.*, **145**(3), 909-919 (1998). https://doi.org/10.1149/1.1838366
[22] F. Lebreau, M.M. Islam, B. Diawara, and P. Marcus, "Structural, magnetic, electronic, defect and diffusion properties of Cr_2O_3: A DFT+*U* study", *J. Phys. Chem., C*, **118**, 18133-18145 (2014). https://doi.org/10.1021/jp5039943
[23] H. Ke, and C.D. Taylor, "DFT-based calculation of dissolution activation energy and kinetics of Ni-Cr alloys", *J. Electrochem. Soc.*, **164**(13), 131508 (2020). https://doi.org/10.1149/1945-7111/abbbbd
[24] Y. Xie, J. Zhang, and D.J. Young, "Temperature effect on oxidation behavior of Ni-Cr alloys in CO_2 gas atmosphere", *J. Electrochem., Soc.*, **164**(6), C285-C293 (2017). https://doi.org/10.1149/2.1021706jes
[25] W.H. Blades, M.R. Barone, and P. Reinke, "Initial atomic-scale oxidation pathways on a Ni-15Cr(100) alloy surface", *npj Mat. Degrad.*, **5**:17 (2021). https://doi.org/10.1038/s41529-021-00164-7
[26] X.-X. Yu, A. Gulec, C.M. Andolina, E.J. Zeitchick, K. Gusieva, J.C. Yang, J.R. Scully, J.H. Perepezko, and L.D. Marks, "In situ observations of early stage oxidation of Ni-Cr and Ni-Cr-Mo alloys", *Corrosion*, **74**(9), 939-946 (2018). https://doi.org/10.5006/2807
[27] X.-X. Yu, J. Han, J.R. Scully, and L.D. Marks, "Oxygen injection during fast vs slow passivation in aqueous solution", *Acta Mat.*, **213**, 116898 (2021). https://doi.org/10.1016/j.actamat.2021.116898
[28] V. Maurice, and P. Marcus, "Current developments of nanoscale insight into corrosion protection by passive oxide films", *Current Opinion in Solid State & Materials Science*, **22**, 156-167 (2018). https://doi.org/10.1016/j.cossms.2018.05.004

[29] S. Boudin, J-.L. Vignes, G. Lorang, M. Da Cunha Belo, G. Blondiaux, S.M. Mikhailov, J.P. Jacobs, and H.H. Bronersma, "Analytical and electrochemical study of passive films formed on nickel-chromium alloys: Influence of the chromium bulk concentration", *Surf. & Inter. Anal.*, **22**, 462-466 (1994).
[30] J.D. Henderson, A. Seyeux, S. Zanna, M.C. Biesinger, D.W. Shoesmith, J.J. Noël, and P. Marcus, "Investigating the transport mechanisms governing the oxidation of Hastelloy BC-1 by in situ ToF-SIMS", *Corros. Sci.*, **159**, 108138 (2019). https://doi.org/10.1016/j.corsci.2019.108138
[31] T. Jabs, P. Borthen, and H.-H. Strehblow, "X-ray photoelectron spectroscopic examinations of electrochemically formed passive layers on Ni-Cr alloys", *J. Electrochem. Soc.*, **144**(4) 1231-1243 (1997).
[32] Z. Wang, C. Carrière, A. Seyeux, S. Zanna, D. Mercier, and P. Marcus, "XPS and ToF-SIMS investigation of native oxides and passive films formed on nickel alloys containing chromium and molybdenum", *J. Electrochem. Soc.*, **168**, 041503 (2021). https://doi.org/10.1149/1945-7111/abf308
[33] J.D. Henderson, X. Li, F.P. Filice, D. Zagidulin, M.C. Biesinger, B. Kobe, D.W. Shoesmith, K. Ogle, and J.J. Noël, "Investigating the role of Mo and Cr during the activation and passivation on Ni-based alloys in acidic chloride solution", *J. Electrochem. Soc.*, **168**(2) 021509 (2021). https://doi.org/10.1149/1945-7111/abe47a
[34] Z. Wang, F. Di-Franco, A. Seyeux, S. Zanna, V. Maurice and P. Marcus, "Passivation-induced physicochemical alterations of the native surface oxide film on 316L austenitic stainless steel", *J. Electrochem. Soc.*, **166**(11), C3376-C3388 (2019). https://doi.org/10.1149/2.0321911jes
[35] L. Wang, D. Mercier, S. Zanna, A. Seyeux, M. Laurent-Brocq, L. Perrière, I. Guillot, and P. Marcus, "Study of the surface oxides and corrosion behaviour of an equiatomic CoCrFeMnNi high entropy alloy by XPs and ToF-SIMS", *Corros. Sci.*, **167**, 108507 (2020). https://doi.org/10.1016/j.corsci.2020.108507
[36] X. Wang, D. Mercier, Y. Danard, T. Rieger, L. Perriere, M. Laurent-Brocq, I. Guillot, V. Maurice, and P. Marcus, "Enhanced passivity of Cr-Fe-Co-Ni-Mo multi-component single-phase face-centred cubic alloys: design, production and corrosion behaviour", *Corros. Sci.*, **200**, 110233 (2022). https://doi.org/10.1016/j.corsci.2022.110233
[37] M. Zietala, T. Durejko, M. Polański, I. Kunce, T. Płociński, W. Zieliński, M. Łazińska, W. Stępniowski, T. Czujko, K.J. Kurzydłowski, and Z. Bojar, "The microstructure, mechanical properties and corrosion resistance of 316 L stainless steel fabricated using laser engineered net shaping", *Mat. Sci. & Engin. A*, **677**, 1-10 (2016). https://dx.doi.org/10.1016/j.msea.2016.09.028
[38] R.I. Revilla, B. Wouters, F. Andreatta, A. Lanzutti, L. Fedrizzi, and I.D. Graeve, "EIS comparative study and critical equivalent electrical circuit (EEC) analysis of the native oxide layer of additive manufactured and wrought 316L stainless steel", *Corros. Sci.*, **167**, 108480 (2020). https://doi.org/10.1016/j.corsci.2020.108480
[39] D.D. Macdonald, "Passivity-the key to our metals-based civilization", *Pure & Appl. Chem.*, **71**(6), 951-978 (1999). https://doi.org/10.1351/pac199971060951
[40] P. Schmuki, "From Bacon to barriers: a review on the passivity of metals and alloys", *J. Solid State Electrochem.*, **6**, 145-164 (2002). https://doi.org/10.1007/s100080100219
[41] A. Larsson, G. D'Qcunto, M. Vorobyova, G. Abbondanza, U. Lienert, Z. Hegedüs, A. Preobrajenski, L.R. Merte, J: Eidhagen, A. Delblanc, J. Pan, and E. Lundgren, "Thickness and composition of native oxides and near-surface regions of Ni superalloys", *J. Alloys & Comp.*, **895**, 165657 (2022). https://doi.org/10.1016/j.jallcom.2021.162657
[42] D. Caplan, A. Harvey, and M. Cohen, "The effect of surface preparation on oxide films on Cr and Fe-Cr alloys", *J. Electrochem. Soc.*, **108** (1961). https://doi.org/10.1149/1.2428028
[43] S. Neupane, S. Zanna, A. Seyeux, L.H. Klein, V. Maurice, and P. Marcus, "Can we enhance passivity with a surface finish? Spectroscopic and electrochemical analysis on 316L stainless steel", *J. Electrochem. Soc.*, **169**, 011505 (2022). https://doi.org/10.1149/1945-7111/ac4bf7
[44] C. Örnek, C. Leygraf, and J. Pan, "Passive film characterization of duplex stainless steel using scanning Kelvin probe force microscopy in combination with electrochemical measurements", *npj Mat. Degrad.*, **3**, 8 (2019). https://doi.org/10.1038/s41529-019-0071-8

[45] K. Rokosz, T. Hryniewicz, and S. Raaen, "Characterization of passive film formed on AISI 316L stainless steel after magnetoelectropolishing in a broad range of polarization parameters", *Steel Research Int.*, **83** (2012) 910-918. https://doi.org/10.1002/srin.201200046
[46] S-.J. Lee, and J-.J. Lai, "The effects of electropolishing (EP) process parameters on corrosion resistance of 316L stainless steel", *J. Mat. Process. Tech.*, **140**(1-3), 206-210 (2003). https://doi.org/10.1016/S0924-0136(03)00785-4
[47] P. Lochynski, S. Charazinska, E. Łyczkowska-Widłak, and A. Sikora, "Electropolishing of stainless steel in laboratory and industrial scale", *Metals*, **9**, 854 (2019). https://doi.org/10.3390/met9080854
[48] S. Yin, J. Cizek, X. Yan, and R. Lupoi, "Annealing strategies for enhancing mechanical properties of addivity manufactured 316L stainless steel deposited by cold spray", *Surf. & Coat. Tech.*, **370**(25), 353-361 (2019). https://doi.org/10.1016/j.surfcoat.2019.04.012
[49] J.S. Park, D.M. Cho, S.G. Hong, and S.J. Kim, "Effects of reducing atmospheres of bright annealing on the surface and corrosion characteristics of super duplex stainless steel tubes", *Surf. & Coat. Tech.*, **423**, 127621 (2021). https://doi.org/10.1016/j.surfcoat.2021.127621
[50] L. Kosec, Š. Šavli, S. Kožuh , T.H. Grgurić, A. Nagode , G. Kosec, G. Dražić, and M. Gojić, "Transformation of austenite during isothermal annealing at 600-900°C for heat-resistant stainless steel", *J. Alloy & Comp.*, **567**, 59-64 (2013). http://doi.org/10.1016/j.jallcom.2013.03.102
[51] C.J. Park, V.S. Rao, and H.S. Kwon, "Effect of sigma phase on the initiation and propagation of pitting corrosion of duplex stainless steel", *Corrosion*, **61**(1), 76-83 (2005). https://doi.org/10.5006/1.3278163
[52] E. Gardin, S. Zanna, A. Seyeux, A. Allion-Maurer, and P. Marcus, "Comparative study of the surface oxide films on lean duplex and corresponding single phase stainless steels by XPs and ToF-SIMS", *Corros. Sci.*, **143**, 403 (2018). https://doi.org/10.1016/j.corsci.2018.08.009
[53] B.J. Brug. A.L.G. Van Den Eeden, M. Sluyters-Rehbach, and J.H. Sluyters, "The analysis of electrode impedance complicated by the present of a constant phase element", *J. Electroanal. Chem.*, **176**, 275-295 (1984); https://doi.org/10.1016/S0022-0728(84)80324-1
[54] M.E. Orazem, N. Pébère, and B. Tribollet, "Enhanced graphical representation of electrochemical impedance data", *J. Electrochem. Soc.*, **153**, B129 (2006). https://doi.org/10.1149/1.2168377
[55] O. Gharbi, M.T.T. Tran, M.E. Orazem, B. Tribollet, M. Turmine, and V. Vivier, "Impedance response of a thin film on an electrode: Deciphering the influence of the double layer capacitance", *Chem. Phys. Chem.*, **22**, 1-9 (2021). https://doi.org/10.1002/cphc.202100177
[56] M. Benoit, C. Bataillon, B. Gwinner, F. Miserque, M.E. Orazem, C.M. Sánchez-Sánchez, B. Tribollet, and V. Vivier, "Comparison of different methods for measuring the passive film thickness on metals", *Electrochim. Acta*, **201**, 340-347 (2016). http://doi.org/10.1016/j.electacta.2015.12.173
[57] A. Seyeux, S. Zanna, A. Allion, P. Marcus, "The fate of the protective oxide film on stainless steel upon early stage growth of a biofilm", *Corros. Sci.*, **91**, 352-356 (2015); https://doi.org/10.1016/j.corsci.2014.10.051
[58] A. Seyeux, Z. Wang, S. Zanna, C. Carrière, D. Mercier, P. Marcus, "ToF-SIMS investigation with ^{18}O isotopic tracer of the ion transport mechanisms in surface oxide on nickel-chromium and nickel-cromium-molybdenum alloys", *Electrochim. Acta*, **426**, 14079 (2022). https://doi.org/10.1016/j.electacta.2022.140797
[59] Z. Wang, C. Carrière, A. Seyeux, S. Zanna, D. Mercier, and P. Marcus, "Thermal stability of surface oxides on nickel alloys (NiCr and NiCrMo) investigated by XPS and ToF-SIMS", *Appl. Surf. Sci.*, **576**, 151836 (2022). https://doi.org/10.1016/j.apsusc.2021.151836
[60] E.J. Kautz, S.V. Lambeets, D.E. Perea, A.Y. Gerard, J. Han, J.R. Scully, J.E. Saal, and D.K. Schreiber, "Elemental redistributions during early stages of oxidation in $Ni_{38}Cr_{22}Fe_{20}Mn_{10}Co_{10}$ multi-principal element alloy", *Scripa Mat.*, **194**, 113609 (2021). https://doi.org/10.1016/j.scriptamat.2020.10.051
[61] A.Y. Gerard, J. Han, S.J. McDonnel, K. Ogle, E.J. Kautz, D.K. Schreiber, P. Lu, J.E. Saal, G.S. Frankel, and J.R. Scully, "Aqueous passivation of multi-principal element alloy $Ni_{38}Fe_{20}Cr_{22}Mn_{10}Co_{10}$:

Unexpected high Cr enrichment within the passive film", *Acta Mat.*, **198**, 121-133 (2020). https://doi.org/10.1016/j.actamat.2020.07.024
[62] T. Gheno, F. Jomard, C. Desgranges, and L. Martinelli, "Tracer diffusion of Cr in Ni and Ni-22Cr studied by SIMS", *Materialia*, **3**, 145-152 (2018). https://doi.org/10.1016/j.mtla.2018.08.004
[63] A. Seyeux, V. Maurice, and P. Marcus, "Oxide film growth kinetics on metals and alloys: I. Physical model", *J. Electrochem. Soc.*, **160**(6), C189 (2013). https://doi.org/10.1149/2.036306jes
[64] C. Zhou, J. Wang, S. Hu, H. Tao, B. Fang, L. Li, J. Zheng, and L. Zhang, "Enhanced corrosion resistance of additively manufactured 316L stainless steel after heat treatment", *J. Electrochem. Soc.*, **167**, 141504 (2020). https://doi.org/10.1149/1945-7111/abc10e
[65] Y.B. Lei, Z.B. Wang, B. Zhang, Z.P. Luo, J. Lu, and K. Lu, "Enhanced mechanical properties and corrosion resistance of 316L stainless steel by pre-forming a gradient nanostructured surface layer and annealing", *Acta Mat.*, **208**, 116773 (2021). https://doi.org/10.1016/j.actamat.2021.116773
[66] M.E. Orazem, and B. Tribollet, "Electrochemical impedance spectroscopy", 2nd ed., John Wiley & Sons, 2017, pp. 201-205.
[67] J. Han, M.G. Wartenberg, H.L. Chan, B.K. Derby, N. Li, and J.R. Scully, "Electrochemical stability, physical, and electronic properties of thermally pre-formed oxide compared to artificially sputtered oxide on Fe thin films in aqueous chloride", *Corros. Sci.*, **186**, 109456 (2021). https://doi.org/10.1016/j.corsci.2021.109456
[68] N.E. Hakiki, J.L. Bubendorff, C. Pirri, F. Mechehoud, A. Mehdaoui, and M. Belhadji, "Electrochemical and structural characterization of nickel based alloys oxides", *Phys. Procedia*, **55**, 243-250 (2014). https://doi.org/10.1016/j.phpro.2014.07.036
[69] M.G.S. Ferreira, M.D.C. Belo, N.E. Hakiki, G. Goodlet, M.F. Montemor, and A.M.P. Simões, "Semiconducting properties of oxide and passive film formed on AISI 304 stainless steel and alloy 600", *J. Braz. Chem. Soc.*, **13**(4), 433-440 (2002). https://doi.org/10.1590/S0103-50532002000400005
[70] D. Zagidulin, X. Zhang, J. Zou, J.J. Noel, and D.W. Shoesmith, "Characterization of surface composition on alloy 22 in neutral chloride solutions", *Surf. & Interface Anal.*, **45**, 1014-1019 (2013). https://doi.org/10.1002/sia.5204
[71] X. Zhang, D. Zagidulin, and D. W. Shoesmith, "Characterization of film properties on the Ni-Cr-Mo alloy C-2000", *Electrochim. Acta*, **89**, 814-822 (2013). https://doi.org/10.1002/sia.5204
[72] S. Liu, C. Yue, X. Chen, Q. Zhu, and Y. Tu, "Pitting corrosion resistance on annealing treated super duplex stainless steel S32750", *Crystals*, **10**, 294 (2020). https://doi.org/10.3390/cryst10040294
[73] X. Yue, L. Zhang, Y. Hua, J. Wang, N. Dong, X. Li, S. Xu, and A. Neville, "Revealing the superior corrosion protection of the passive film on selective laser melted 316L SS in a phosphate-buffered saline solution", *Appl. Surf. Sci.*, **529**, 147170 (2020). https://doi.org/10.1016/j.apsusc.2020.147170
[74] C.-O.A. Olsson, and D. Landolt, "Passive films on stainless steels – chemistry, structure and growth", *Electrochim. Acta*, **48**, 1093-1104 (2003). https://doi.org/10.1016/S0013-4686(02)00841-1
[75] B. Hirschorn, M.E. Orazem, B. Tribollet, V. Vivier, I. Frateur, and M. Musiani, "Constant-phase-element behavior caused by resistivity distributions in films", *J. Electrochem. Soc.*, **157**(12), C458-C463 (2010). https://doi.org/10.1149/1.3499565
[76] S. Marcelin, Z. Zhang, B. Ter-Ovanessian, and B. Normand, "Relationship between the resistivity profiles obtained from the power law model and the physico-chemical properties of passive films", *J. Electrochem. Soc.*, **168**, 021503 (2021). https://doi.org/10.1149/1945-7111/abde84
[77] M.E. Orazem, B. Tribollet, V. Vivier, D.P. Riemer, E. White, and A. Bunge, "On the use of the power-law model for interpreting constant-phase-element parameters", *J. Braz. Chem. Soc.*, **25**(3), 532-539 (2014). http://doi.org/10.5935/0103-5053.20140021